PHOTONICS Research

Nonsuspended optomechanical crystal cavities using As_2S_3 chalcogenide glass

Renduo Qi,[1] Qiancheng Xu,[1] Ning Wu,[1] Kaiyu Cui,[1,2,3] Wei Zhang,[1,2,3,*] and Yidong Huang[1,2,3]

[1]Beijing National Research Center for Information Science and Technology (BNRist), Beijing Innovation Center for Future Chips, Electronic Engineering Department, Tsinghua University, Beijing 100084, China
[2]Frontier Science Center for Quantum Information, Beijing 100084, China
[3]Beijing Academy of Quantum Information Sciences, Beijing 100193, China
*Corresponding author: zwei@tsinghua.edu.cn

Received 18 December 2020; revised 19 March 2021; accepted 21 March 2021; posted 22 March 2021 (Doc. ID 417933); published 30 April 2021

An optomechanical crystal cavity with nonsuspended structure using As_2S_3 material is proposed. The principle of mode confinement in the nonsuspended cavity is analyzed, and two different types of optical and acoustic defect modes are calculated through appropriate design of the cavity structure. An optomechanical coupling rate of 82.3 kHz is obtained in the proposed cavity, and the designed acoustic frequency is 3.44 GHz. The acoustic mode coupling between two nonsuspended optomechanical crystal cavities is also demonstrated, showing that the proposed cavity structure has great potential for realizing further optomechanical applications in multicavity systems.

https://doi.org/10.1364/PRJ.417933

1. INTRODUCTION

Cavity optomechanics explores the interaction between optical and mechanical modes in optical/mechanical resonance systems, and it is promising for a wide range of applications such as high-precision sensing [1–3], laser cooling [4], and nonreciprocal devices [5,6]. Various microcavity systems have been investigated for cavity optomechanics, including microtoroids [7], microdisks [8], and optomechanical crystal cavities [9–13]. Among these systems, optomechanical crystal cavities have attracted much attention because of their smaller mode volumes and higher optomechanical coupling rates [14,15]. So far, silicon is the dominant material for optomechanical crystal cavities, which are usually fabricated on silicon-on-insulator (SOI) substrates. However, since the sound velocity in silicon is larger than that in silica, it is hard to confine acoustic modes in the silicon layers [16]. Therefore, suspended cavity structures are required in these systems to confine the acoustic modes and enhance the overlap between optical and acoustic modes. However, the suspended structures would increase the difficulty of fabrication and limit the structural complexity of the devices. In addition, extra structure designs are required in the suspended cavity systems to realize further functions such as acoustic mode coupling [17,18].

Recently, chalcogenide glasses (ChGs) have drawn a lot of interest in nonlinear optics because of their large Kerr nonlinearity as well as low two-photon absorption [19,20]. More importantly, these materials have relatively high refractive index and low sound velocity, so that both optical modes and acoustic modes can be confined in the ChG core without using suspended structures [21]. Based on this feature, different integrated ChG devices have been fabricated for applications such as stimulated Brillouin scattering [22–24], which also results from the interaction between photons and phonons in traveling acoustic modes. Therefore, it could be expected to achieve effective optomechanical coupling based on nonsuspended ChG devices. The nonsuspended structures have the advantage of more flexible designs, and they can directly realize functions such as acoustic mode coupling among cavity arrays and external modulations without extra structures.

In this work, a nonsuspended optomechanical crystal cavity using As_2S_3 material with nanobeam structure is proposed. Theoretical analysis shows that both optical and acoustic modes are well confined in the cavity by adjusting and optimizing the structural parameters. Two different types of optical and acoustic defect modes are calculated, and an optomechanical coupling rate of 82.3 kHz is obtained. The coupling of acoustic modes between two nonsuspended optomechanical crystal cavities is also demonstrated, showing that the proposed cavity structure has great potential in realizing complex optomechanical functions.

2. CAVITY STRUCTURE AND MODE ANALYSIS

A. Cavity Design

The top view schematic of the proposed nonsuspended As_2S_3 optomechanical crystal cavity is shown in Fig. 1(a). It consists of a strip nanobeam of As_2S_3 material and a row of holes filled

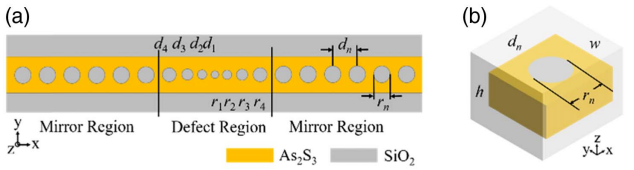

Fig. 1. (a) The top view schematic of the nonsuspended As_2S_3 optomechanical crystal cavity. (b) A unit cell of the optomechanical crystal in the mirror region.

with silica, while the whole structure is embedded in silica cladding. A possible fabrication method for this structure is microtrench filling and lift-off process [25], followed by the deposition of silica upper cladding. Figure 1(b) shows a unit cell of the structure. The width and height of the As_2S_3 beam are denoted by w and h, respectively. The radius of silica holes (r_n) and the lattice constant of the unit cell (d_n) are invariant in the mirror region, which acts as a periodic structure to reflect both optical and acoustic fields. In the defect region, the radii of holes (r_1–r_4) and the lattice constants (d_1–d_4) vary linearly to trap both optical and acoustic defect modes into the center of the cavity. The light coupling of the optical defect mode in the embedded cavity structure could be achieved by evanescent field coupling through an on-chip waveguide placed beside the cavity.

B. Optical and Acoustic Defect Modes at the X Point

To analyze how the defect modes are confined in the cavity, the optical and acoustic bands of the one-dimensional periodic structure in the mirror region are calculated. The structural parameters used in the calculation are shown in the second column of Table 1. The refractive indices of As_2S_3 and silica are set to be 2.45 and 1.44, respectively. Figure 2(a) shows the optical band of TE modes calculated by the plane-wave expansion method. The blue line indicates the dispersion of uniform plane waves in the near-infrared band traveling in the surrounding material, which is silica in the proposed structure. The guided optical modes are located below the light line of silica, and an optical band gap between 188 and 210 THz is generated in the grey region of the optical band diagram. Therefore, by adjusting the radii of holes and lattice constants in the defect region, an optical defect mode within the band gap is introduced into the structure. The defect mode is confined by the optomechanical crystal in the x direction and by refractive index guiding in the y and z directions. The optical defect mode is calculated using the finite element method (FEM), and the electric field component E_y of the mode is shown in Fig. 2(c). The frequency of the mode is 193 THz, and

Table 1. Structural Parameters of the Cavity

Parameter	Modes at the X point	Modes at the Γ point
r_1	85 nm	113 nm
r_n	147 nm	135 nm
d_1	416 nm	811 nm
d_n	466 nm	830 nm
w	557 nm	609 nm
t	374 nm	400 nm

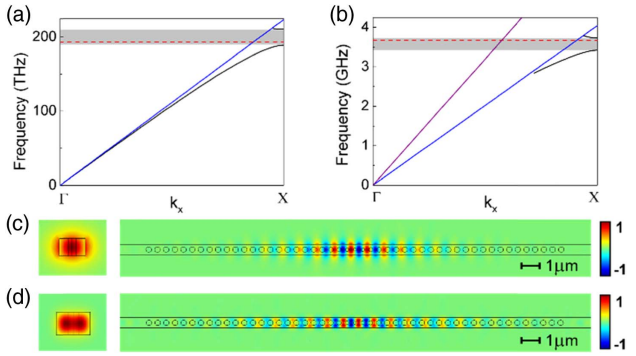

Fig. 2. (a) Optical band structure of the unit cell in the mirror region. (b) Acoustic band structure of the unit cell in the mirror region. (c) Electric field component E_y of the optical defect mode at the X point. Left: distribution of E_y at plane $x = d_1/2$. Right: distribution of E_y at plane $z = 0$. [The coordinate of the cavity center is set as (0,0,0).] (d) Displacement field component u_x of the acoustic defect mode at the X point. Left: distribution of u_x at plane $x = d_1/2$. Right: distribution of u_x at plane $z = 0$.

the Q factor is 8600 with 20 periods of optomechanical crystals in the mirror region. The confinement of the optical mode is relatively weak since the refractive index difference between As_2S_3 and silica is not as large as the difference between silicon and air.

The acoustic band of the periodic structure is then calculated using FEM. In the calculation, the unit cell is set with Bloch boundary condition in the x direction. The density, Young's modulus, and Poisson's ratio of As_2S_3 and silica are set to be 3200 kg/m^3, 16 GPa, 0.24 and 2200 kg/m^3, 73.1 GPa, 0.17, respectively [16,26]. Figure 2(b) shows the calculated acoustic bands of y- and z-symmetric modes using the structural parameters mentioned above. In the nonsuspended cavity, acoustic defect modes may couple with the acoustic waves in the surrounding material, leading to field leakage. The blue line and purple line in Fig. 2(b) indicate the dispersion lines of transverse waves and longitudinal waves in silica, respectively. The acoustic modes below both of the lines are guided modes, and an acoustic band gap is generated between 3.42 and 3.73 GHz. Figure 2(d) shows the displacement field component u_x of the acoustic defect mode. The component u_x is chosen for plotting since it has the most overlap with the electric field, resulting in a dominant contribution to the optomechanical coupling rate. The frequency of the mode is 3.67 GHz, which is indicated by the red dashed line in the acoustic band diagram. The calculated Q factor of the mode with 20 periods of optomechanical crystals in the mirror region is 1000. It is worth noting that the Q factors of the investigated acoustic mode under different numbers of periods are also calculated. Results show that when the number of periods is relatively small, the Q factor rises with increasing number of periods, and the overall loss is mainly composed of losses through the mirror regions. Then the Q factor stops increasing and remains almost unchanged after the number of periods reaches 20. It indicates that the vertical losses into the surrounding cladding start to dominate when the number of periods is over 20.

The optomechanical coupling rate describes the interaction strength between optical and mechanical modes. It is defined as the optical frequency shift induced by the zero-point displacement of the mechanical mode and can be expressed by the following equation [27]:

$$g = \frac{\partial \omega_0}{\partial \alpha} x_{\mathrm{zpf}}, \tag{1}$$

where ω_0 is the angular frequency of the optical mode, α is the normalized amplitude of the displacement field, and x_{zpf} is the zero-point motion of the acoustic mode. It can be calculated by considering the contributions from moving boundary (MB) [28] and photoelastic (PE) effects [29]. The optomechanical coupling rate due to the moving boundary effect is expressed as [30]

$$g_{\mathrm{MB}} = -\frac{\omega_0}{2} \frac{\oint (\mathbf{q} \cdot \hat{\mathbf{n}})(\Delta\varepsilon \mathbf{E}_{\parallel}^2 - \Delta\varepsilon^{-1} \mathbf{D}_{\perp}^2) \mathrm{d}S}{\int \mathbf{E} \cdot \mathbf{D} \mathrm{d}V} x_{\mathrm{zpf}}, \tag{2}$$

where $\mathbf{q}$ is the normalized displacement field of the acoustic mode, $\hat{\mathbf{n}}$ is the unit surface normal vector, $\mathbf{E}_{\parallel}$ is the parallel component of the electric field, $\mathbf{D}_{\perp}$ is the perpendicular component of the electric displacement field, ε is the material permittivity, and $\Delta\varepsilon$ and $\Delta\varepsilon^{-1}$ are defined as $\varepsilon_{As_2S_3} - \varepsilon_{SiO_2}$ and $\varepsilon^{-1}_{As_2S_3} - \varepsilon^{-1}_{SiO_2}$, respectively. The photoelastic effect occurs in both the As_2S_3 and silica regions of the cavity, and the contribution to the coupling rate is given by [14]

$$g_{\mathrm{PE}} = -\frac{\omega_0 \varepsilon_0 n^4}{2} \frac{\langle \mathbf{E} | \mathbf{p} : \mathbf{S} | \mathbf{E} \rangle}{\int \mathbf{E} \cdot \mathbf{D} \mathrm{d}V} x_{\mathrm{zpf}}, \tag{3}$$

where ε_0 is the vacuum permittivity, n is the material refractive index, $\mathbf{S}$ is the strain tensor, and $\mathbf{p}$ is the photoelastic tensor. The photoelastic coefficients (p_{11}, p_{12}, p_{44}) are (0.308, 0.299, 0) for As_2S_3 and (0.121, 0.27, −0.075) for silica [31].

To optimize the cavity design, an algorithm based on simulated annealing is used to achieve the maximum optomechanical coupling rate. The six independent geometric parameters for optimization are (r_1, r_n, d_1, d_n, w, h), and the optimized results are shown in the second column of Table 1. The optomechanical coupling rate of the cavity is calculated to be $g_0/2\pi = 2.5$ kHz, composed of −0.6 kHz from the moving boundary effect and 3.1 kHz from the photoelastic effect. The obtained coupling rate is relatively low compared to the coupling rate of suspended nanobeam cavities. It is due to the canceling of the optomechanical coupling rate contribution from two adjacent unit cells. Taking the photoelastic effect for example, the coupling rate caused by the photoelastic effect is proportional to the integral of the strain field of the acoustic mode and the square of the electric field of the optical mode. For the modes at the X point of the band diagram, the electric field and strain field in two adjacent unit cells have the opposite phase. Therefore, the contributions of coupling rate from two adjacent unit cells have different signs and cancel each other out, resulting in a relatively low coupling rate of the whole structure.

C. Optical and Acoustic Defect Modes at the Γ Point

To increase the optomechanical coupling rate of the nonsuspended optomechanical crystal cavity, we investigate another type of acoustic modes, which are at the Γ point of the band diagram. For these modes, the phases of the displacement field in different unit cells are consistent with each other, and the contribution of coupling rate can be superimposed. In the proposed nonsuspended cavity, most modes at the Γ point are leaky modes and cannot satisfy the total internal reflection condition in the y and z directions due to the existence of silica cladding. Nevertheless, some specific modes at the Γ point can be well confined in the cavity though they are above the dispersion line of plane waves in the silica cladding, since

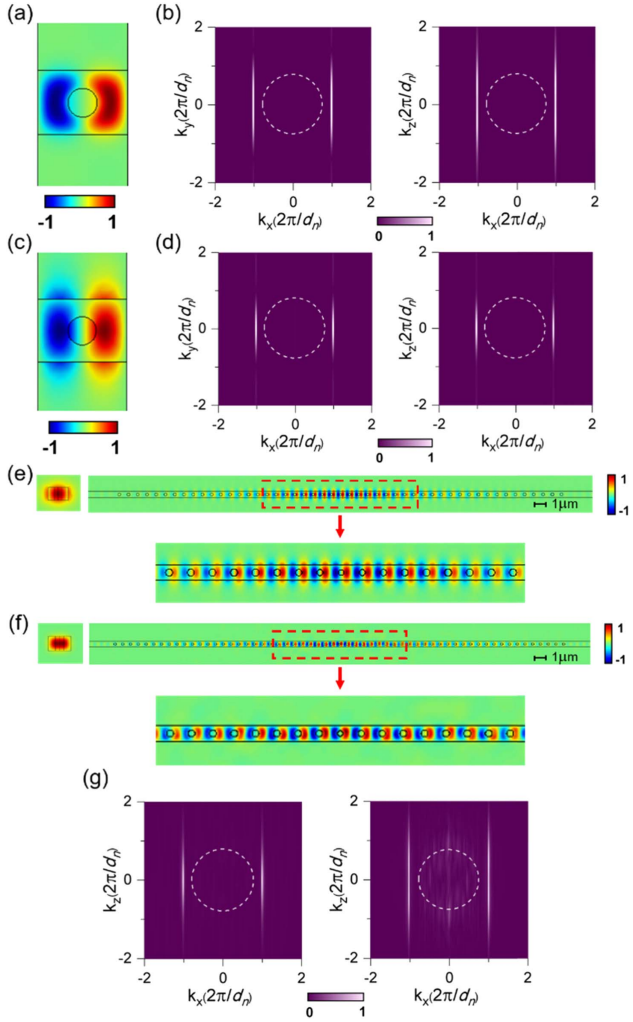

Fig. 3. (a) Displacement field profile (u_x) of a confined acoustic Bloch mode at the Γ point. (b) 2D FT spectrum of u_x of the acoustic Bloch mode at the cavity interface perpendicular to the z direction (left) and interface perpendicular to the y direction (right). (c) Electric field profile (E_y) of a confined optical Bloch mode at the Γ point. (d) 2D FT spectrum of E_y of the optical Bloch mode at the cavity interface perpendicular to the z direction (left) and interface perpendicular to the y direction (right). (e) Electric field component E_y of the optical defect mode at the Γ point. Left: distribution of E_y at plane $x = d_1/4$. Right: distribution of E_y at plane $z = 0$. (f) Displacement field component u_x of the acoustic defect mode at the Γ point. Left: distribution of u_x at plane $x = d_1/4$. Right: distribution of u_x at plane $z = 0$. (g) 2D FT spectrum of E_y of the optical defect mode at the cavity interface perpendicular to the y direction (left). 2D FT spectrum of u_x of the acoustic defect mode at the cavity interface perpendicular to the y direction (right).

most plane wave components of these modes are mismatched with the plane waves in silica [32,33]. Accordingly, we calculate the acoustic Bloch modes of a unit cell around the Γ point with the structural parameters provided in the third column of Table 1. Figure 3(a) shows the displacement field profile of a well-confined Bloch mode with $k_x = 0$. The displacement field component u_x at the interfaces between As_2S_3 and silica is decomposed into plane wave components by Fourier transformation (FT), and the results are shown in Fig. 3(b). It can be seen that most components of the Bloch mode are outside the white circle, which represents the equal frequency surface of the transverse acoustic waves in bulk silica material. Therefore, this mode has little coupling with the plane waves in silica and is confined in the nonsuspended cavity. However, we find that it is hard to confine the acoustic mode at the Γ point and optical modes at the X point simultaneously due to the relatively small band gap of the nonsuspended optomechanical crystal and the limited geometrical degrees of freedom in the cavity structure. Therefore, it is also necessary to employ optical modes at the Γ point for better mode confinement. Figure 3(c) shows the electric field profile of an optical Bloch mode at the Γ point. The electric field component E_y at interfaces between As_2S_3 and silica is also decomposed into plane wave components by Fourier transformation, and the results are shown in Fig. 3(d). Most of the plane wave components are outside the white light cone, indicating that the optical mode is also well confined in the cavity.

Through appropriate design of the cavity structure, the optical and acoustic defect modes at the Γ point can be supported by the cavity. Figures 3(e)–3(f) are the calculated optical and acoustic defect mode profiles. The frequency and calculated Q factor of the optical and acoustic modes are 196.8 THz, 3000 and 3.44 GHz, 500, respectively, with 20 periods of unit cells in each mirror region. We also calculate the Q factors of the acoustic mode at the Γ point under different numbers of periods in the mirror regions. It shows that the Q factor stops increasing and remains almost unchanged with the number of periods when it is over 20, like the case of the acoustic mode at the X point. The FT spectra of the defect optical and acoustic modes at the cavity interfaces are shown in Fig. 3(g). The optomechanical coupling rate between these two modes is calculated to be 82.3 kHz, which is much higher than the coupling rate of the cavity supporting optical and acoustic modes at the X point. Simulation results show that the coupling rate between these two modes at the Γ point is also dominated by the contribution of u_x.

3. INTERCAVITY ACOUSTIC MODE COUPLING

In optomechanical systems, the acoustic coupling between cavities is significant to realize complex optomechanical functions, such as dynamic entanglement transfer and the mechanical parity-time symmetry effect [17,34,35]. For suspended nanobeam systems, the acoustic modes of different cavities cannot couple with each other directly and thus require extra nanowires or acoustic waveguides to introduce acoustic coupling into the systems [17,18]. In contrast, the acoustic coupling between cavities of the nonsuspended optomechanical crystal systems can be realized directly through the cladding without extra structure designs. To demonstrate the acoustic coupling condition of the nonsuspended optomechanical crystal cavities, a dual-cavity system containing two identical cavities with a separation distance L is analyzed as shown in Fig. 4(a). The structural parameters are set to confine the optical and acoustic modes at the X point as listed in Table 1. Two supermodes, including an even mode and an odd mode, are calculated in the system, and their profiles are plotted in Fig. 4(b). The acoustic coupling rate can be obtained as half of the frequency difference between the two supermodes. The coupling rates under different distances between the two cavities are calculated and plotted as the black solid line in Fig. 4(b). It indicates that effective acoustic coupling is realized as two cavities approach each other, and a coupling rate of 300 kHz is achieved under the distance of 2 μm.

In some applications, the optical coupling between cavities is not expected while acoustic coupling is required. It can be realized by tuning the optical frequency of one cavity while keeping the acoustic frequency unchanged, so that optical coupling could not occur due to the inconsistent optical frequencies of the two cavities. A possible way to realize this is to adjust the radii of silica holes and lattice constants in the defect region of one cavity. The black dashed line in Fig. 4(c) shows the calculated acoustic coupling rates between two nonsuspended optomechanical crystal cavities with different structural parameters. These two cavities have the same acoustic frequency, while the optical frequencies are 193 THz and 197 THz, respectively. The result shows that acoustic mode coupling also occurs on this condition. The optical coupling rates between two cavities are also calculated and plotted in Fig. 4(c). The red solid line indicates the optical coupling rate between two identical cavities, and the red dashed line is the coupling rate between cavities with different optical frequencies. It can be seen that optical mode coupling could be suppressed by this

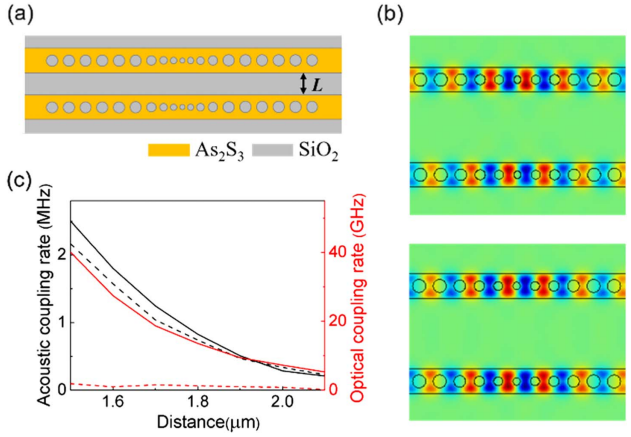

Fig. 4. (a) A dual-cavity system of nonsuspended As_2S_3 optomechanical crystal cavities with a separation distance L. (b) Profiles of the calculated supermodes in the dual-cavity system. Top: the odd mode. Bottom: the even mode. (c) Left ordinate: calculated acoustic coupling rates between two identical cavities (black solid line) and between two different cavities with the same acoustic frequency (black dashed line). Right ordinate: optical coupling rates between two identical cavities (red solid line) and between two different cavities with the same acoustic frequency (red dashed line).

way, while the acoustic mode coupling condition remains almost unchanged.

4. CONCLUSION

In this paper, we have proposed a nonsuspended As_2S_3 optomechanical crystal cavity. The core of the cavity is an As_2S_3 nanobeam structure, and the whole cavity is surrounded by silica cladding. Different optical and acoustic defect modes are supported in the cavity with proper structural design. Optical and acoustic modes at the X point and Γ point of the band diagram are analyzed. The designed acoustic mode at the Γ point has a frequency of 3.44 GHz, and an optomechanical coupling rate of 82.3 kHz is obtained. The Q factors of the modes and the coupling rates could be improved by further optimization of the cavity design. In addition, acoustic mode coupling between two nonsuspended optomechanical crystal cavities is realized directly without extra structures. The calculation results show that the proposed nonsuspended cavities have great potential for realizing further optomechanical applications in multicavity systems.

Funding. National Key Research and Development Program of China (2018YFB2200400); Beijing Municipal Natural Science Foundation (Z180012); National Natural Science Foundation of China (61775115, 61875101, 91750206); Beijing Academy of Quantum Information Sciences (Y18G26); Tsinghua University Initiative Scientific Research Program.

Disclosures. The datasets generated or analyzed during the current study are available from the corresponding author on reasonable request.

REFERENCES

1. A. G. Krause, M. Winger, T. D. Blasius, Q. Lin, and O. Painter, "A high-resolution microchip optomechanical accelerometer," Nat. Photonics **6**, 768–772 (2012).
2. E. Gavartin, P. Verlot, and T. J. Kippenberg, "A hybrid on-chip optomechanical transducer for ultrasensitive force measurements," Nat. Nanotechnol. **7**, 509–514 (2012).
3. Y. Chen, W. S. Fegadolli, W. M. Jones, A. Scherer, and M. Li, "Ultrasensitive gas-phase chemical sensing based on functionalized photonic crystal nanobeam cavities," ACS Nano **8**, 522–527 (2014).
4. Y. C. Liu, Y. F. Xiao, X. Luan, and C. W. Wong, "Dynamic dissipative cooling of a mechanical resonator in strong coupling optomechanics," Phys. Rev. Lett. **110**, 153606 (2013).
5. S. Manipatruni, J. T. Robinson, and M. Lipson, "Optical nonreciprocity in optomechanical structures," Phys. Rev. Lett. **102**, 213903 (2009).
6. F. Ruesink, M. A. Miri, A. Alù, and E. Verhagen, "Nonreciprocity and magnetic-free isolation based on optomechanical interactions," Nat. Commun. **7**, 13662 (2016).
7. M. Hossein-Zadeh and K. J. Vahala, "Observation of optical spring effect in a microtoroidal optomechanical resonator," Opt. Lett. **32**, 1611–1613 (2007).
8. X. Sun, X. Zhang, and H. X. Tang, "High-Q silicon optomechanical microdisk resonators at gigahertz frequencies," Appl. Phys. Lett. **100**, 173116 (2012).
9. M. Eichenfield, J. Chan, R. M. Camacho, K. J. Vahala, and O. Painter, "Optomechanical crystals," Nature **462**, 78–82 (2009).
10. J. Gomis-Bresco, D. Navarro-Urrios, M. Oudich, S. El-Jallal, A. Griol, D. Puerto, E. Chavez, Y. Pennec, B. Djafari-Rouhani, F. Alzina, A. Martínez, and C. M. S. Torres, "A one-dimensional optomechanical crystal with a complete phononic band gap," Nat. Commun. **5**, 4452 (2014).
11. X. Zhang, G. Zhou, P. Shi, H. Du, T. Lin, J. Teng, and F. S. Chau, "On-chip integrated optofluidic complex refractive index sensing using silicon photonic crystal nanobeam cavities," Opt. Lett. **41**, 1197–1200 (2016).
12. S. C. Wu, L. G. Qin, J. Jing, T. M. Yan, J. Lu, and Z. Y. Wang, "Microwave-controlled optical double optomechanically induced transparency in a hybrid piezo-optomechanical cavity system," Phys. Rev. A **98**, 013807 (2018).
13. W. Jiang, R. N. Patel, F. M. Mayor, T. P. McKenna, P. Arrangoiz-Arriola, C. J. Sarabalis, J. D. Witmer, R. V. A. N. Laer, and A. H. Safavi-Naeini, "Lithium niobate piezo-optomechanical crystals," Optica **6**, 845–853 (2019).
14. J. Chan, A. H. Safavi-Naeini, J. T. Hill, S. Meenehan, and O. Painter, "Optimized optomechanical crystal cavity with acoustic radiation shield," Appl. Phys. Lett. **101**, 081115 (2012).
15. Y. Li, K. Cui, X. Feng, Y. Huang, Z. Huang, F. Liu, and W. Zhang, "Optomechanical crystal nanobeam cavity with high optomechanical coupling rate," J. Opt. **17**, 045001 (2015).
16. C. J. Sarabalis, J. T. Hill, and A. H. Safavi-Naeini, "Guided acoustic and optical waves in silicon-on-insulator for Brillouin scattering and optomechanics," APL Photon. **1**, 071301 (2016).
17. Z. Feng, J. Ma, and X. Sun, "Parity–time-symmetric mechanical systems by the cavity optomechanical effect," Opt. Lett. **43**, 4088–4091 (2018).
18. K. Fang, M. H. Matheny, X. Luan, and O. Painter, "Optical transduction and routing of microwave phonons in cavity-optomechanical circuits," Nat. Photonics **10**, 489–496 (2016).
19. B. J. Eggleton, B. Luther-Davies, and K. Richardson, "Chalcogenide photonics," Nat. Photonics **5**, 141–148 (2011).
20. T. Wang, X. Gai, W. Wei, R. Wang, Z. Yang, X. Shen, S. Madden, and B. Luther-Davies, "Systematic z-scan measurements of the third order nonlinearity of chalcogenide glasses," Opt. Mater. Express **4**, 1011–1022 (2014).
21. C. G. Poulton, R. Pant, and B. J. Eggleton, "Acoustic confinement and stimulated Brillouin scattering in integrated optical waveguides," J. Opt. Soc. Am. B **30**, 2657–2664 (2013).
22. R. Pant, C. G. Poulton, D.-Y. Choi, H. Mcfarlane, S. Hile, E. Li, L. Thevenaz, B. Luther-Davies, S. J. Madden, and B. J. Eggleton, "On-chip stimulated Brillouin scattering," Opt. Express **19**, 8285–8290 (2011).
23. M. Merklein, I. V. Kabakova, T. F. S. Büttner, D. Y. Choi, B. Luther-Davies, S. J. Madden, and B. J. Eggleton, "Enhancing and inhibiting stimulated Brillouin scattering in photonic integrated circuits," Nat. Commun. **6**, 6396 (2015).
24. B. J. Eggleton, C. G. Poulton, and R. Pant, "Inducing and harnessing stimulated Brillouin scattering in photonic integrated circuits," Adv. Opt. Photon. **5**, 536–587 (2013).
25. C. Li, P. Guo, W. Huang, W. Zhang, P. Xu, and P. Zhang, "Reverse-strip-structure $Ge_{28}Sb_{12}Se_{60}$ chalcogenide glass waveguides prepared by micro-trench filling and lift-off," J. Opt. Soc. Am. B **37**, 82–87 (2020).
26. J. S. Sanghera, L. B. Shaw, and I. D. Aggarwal, "Applications of chalcogenide glass optical fibers," C. R. Chim. **5**, 873–883 (2002).
27. M. Aspelmeyer, T. J. Kippenberg, and F. Marquardt, "Cavity optomechanics," Rev. Mod. Phys. **86**, 1391–1452 (2014).
28. S. G. Johnson, M. Ibanescu, M. A. Skorobogatiy, O. Weisberg, J. D. Joannopoulos, and Y. Fink, "Perturbation theory for Maxwell's equations with shifting material boundaries," Phys. Rev. E **65**, 066611 (2002).
29. D. K. Biegelsen, "Photoelastic tensor of silicon and the volume dependence of the average gap," Phys. Rev. Lett. **32**, 1196–1199 (1974).
30. A. H. Safavi-Naeini and O. Painter, "Design of optomechanical cavities and waveguides on a simultaneous bandgap phononic-photonic crystal slab," Opt. Express **18**, 14926–14943 (2010).
31. R. W. Dixon, "Photoelastic properties of selected materials and their relevance for applications to acoustic light modulators and scanners," J. Appl. Phys. **38**, 5149–5153 (1967).

32. Y. Akahane, T. Asano, B. S. Song, and S. Noda, "High-*Q* photonic nanocavity in a two-dimensional photonic crystal," Nature **425**, 944–947 (2003).
33. T. Xu, M. S. Wheeler, S. V. Nair, H. E. Ruda, M. Mojahedi, and J. S. Aitchison, "Highly confined mode above the light line in a two-dimensional photonic crystal slab," Appl. Phys. Lett. **93**, 241105 (2008).
34. T. Huan, R. Zhou, and H. Ian, "Dynamic entanglement transfer in a double-cavity optomechanical system," Phys. Rev. A **92**, 022301 (2015).
35. U. S. Sainadh and A. Narayanan, "Mechanical switch for state transfer in dual-cavity optomechanical systems," Phys. Rev. A **88**, 033802 (2013).